Research Article Wiley Online Library ELECTROANALYSIS

doi.org/10.1002/elan.202200159

Electrochemical Tau Protein Immunosensor Based on MnS/GO/PANI and Magnetite-incorporated Gold Nanoparticles

Bahar Bankoğlu Yola,[a] Ceren Karaman,[b] Nermin Özcan,[c] Necip Atar,[d] İlknur Polat,[e] and Mehmet Lütfi Yola*[e]

Abstract: Herein, electrochemical tau protein immunosensor based on manganese sulfide nanoparticles/graphene oxide/polyaniline (MnS/GO/PANI) and magnetite-incorporated gold nanoparticles (AuNPs@Fe_3O_4) was constructed. After the modification of the glassy carbon electrode (GCE) with MnS/GO/PANI, the immobilization and conjugation of anti-Tau capture antibody and antigen Tau protein were successfully completed on MnS/GO/PANI/GCE, respectively. Then, the conjugation of anti-Tau secondary antibody was carried out to AuNPs@Fe_3O_4 as signal amplification via amino-gold affinity and the eventual immunosensor was accomplished by the distinctive interactions of electrode platform and signal amplification. Final immunosensor demonstrated the quantification limit (LOQ) of 1.0×10^{-13} M and the detection limit (LOD) of 1.0×10^{-14} M.

Keywords: Alzheimer's disease · Diagnosis · Voltammetry · Nanocomposite · Detection

1 Introduction

Alzheimer's disease is a neurological disorder that has no effective treatment or early prevention, and it has a detrimental effect on people's daily lives [1]. Neurophysiological tests are commonly used in disease diagnosis, and they are primarily based on detecting clinical symptoms that appear only after permanent brain damage has occurred [2]. Despite recent advances in neuroimaging techniques, there is still a pivotal need for effective and rapid diagnostic kits that can be used for disease early diagnosis [3].

According to current studies, one of the main biomarkers that can be used in the effective diagnosis of Alzheimer's disease is the tau protein, which is generally found in the cerebrospinal fluid and ensures the dynamism and stability of the neural system by binding the neuronal microtubules [4,5]. Some neuropsychological tests and neuroimaging techniques can be employed to examine biomarkers in cerebrospinal fluid quantitatively [6]. However, these techniques have many disadvantages such as high cost, not being available in all health care centers, time-consuming, and being performed with invasive methods, so their widespread use is limited [6]. However, rather than the diagnostic methods that can be performed using cerebrospinal fluid, blood plasma can be considered a suitable medium for the detection of these biomarkers [7]. Even so, since the concentration of biomarkers in blood plasma can be 100 times lower than in cerebrospinal fluid, it can be emphasized that it's imperative to adopt a precise and reliable diagnostic procedure [8].

Currently, some conventional techniques such as enzyme-linked immunosorbent assay, infrared spectroscopy, superconducting quantum interference device, mass spectrometry, surface plasmon resonance, etc. have been employed to detect tau protein [9–11]. These procedures, on the other hand, are sometimes difficult to apply, expensive, time-consuming, or have low sensitivity. Therefore, it is crucial for developing alternative cost- and time-effective methods to monitor tau proteins with high sensitivity even at low concentrations [11]. In this regard, electrochemical sensors have been considered as one of the most viable options in sensitive monitoring biomarkers to diagnose special diseases. Specifically, thanks to their swift response time and ease of scalability, the utilization of electrochemical immunosensors is a favor-

[a] B. B. Yola
Gaziantep Islam Science and Technology University, Faculty of Engineering and Natural Sciences, Department of Engineering Basic Sciences, Gaziantep, Turkey
[b] C. Karaman
Akdeniz University, Vocational School of Technical Sciences, Department of Electricity and Energy, Antalya, Turkey
[c] N. Özcan
Iskenderun Technical University, Faculty of Engineering and Natural Sciences, Department of Biomedical Engineering, Hatay, Turkey
[d] N. Atar
Pamukkale University, Faculty of Engineering, Department of Chemical Engineering, Denizli, Turkey
[e] İ. Polat, M. L. Yola
Hasan Kalyoncu University, Faculty of Health Sciences, Department of Nutrition and Dietetics, Gaziantep, Turkey
Tel.: +903422118080
Fax: +903422118081
E-mail: mlutfi.yola@hku.edu.tr

Supporting information for this article is available on the WWW under https://doi.org/10.1002/elan.202200159

able solution [12–14]. Their electroanalytical performance can be remarkably boosted by tuning the surface of the electrode. The electrode modification with nanomaterials is one of the viable modification approaches to enhance the electrochemical activity of the sensor [15–17].

In recent years, among the various types of nanomaterials, transition metal sulfides have started to attract much attention for electrochemical applications owing to better electric conductivity in comparison with oxides [18,19]. The metal sulfides such as Ni_2S, and MoS_2 have been utilized for electrode materials. Among these metal sulfides, MnS is an additional electrode material owing to its easy availability and abundance [20]. Especially, different forms such as monodispersed hollow nanosphere and tetrapod nanorod crystals are used for the free aqueous procedure. MnS nanocrystals are used as electrochemical electrodes and supercapacitor materials owing to their high conductivity. To increase specific electrode surface area and electrochemical conductivity, the complex formation between graphene oxide and MnS crystal is a significant experimental process. In addition, some new hierarchical structures can provide synergistic interactions between the nanostructures [21]. Especially, 2D graphene materials can be used as a platform in the preparation of nanocomposite materials, indicating a more efficient electrolyte/electrode interface [22]. For instance, the prepared α-MnS/rGO/α-Fe_2O_3/rGO material was utilized in supercapacitors due to the wider electrochemical potential window (+1.6 V) in presence of KOH electrolyte with a capacitance of 161.7 $F g^{-1}$ at a current density of 1.0 $A g^{-1}$ [23]. In another study, ɣ-MnS/reduced graphene oxide nanocomposite was applied to one-pot aqueous technique with a capacitance of 547.6 $F g^{-1}$ at a current density of 1.0 $A g^{-1}$, indicating superior electrochemical stability and reversibility [24].

Some conducting polymers such as polyaniline (PANI) and polythiophene can be used in electrochemical applications including energy storage owing to π-conjugated polymer chains [25]. When the electrochemical oxidation process occurs, the charge density can move towards the polymer sheet, enabling easy electron transfer on the electrode surface. In addition, the dopping process can suggest prominent electrochemical capacitance. Especially, PANI plays an important role in energy storage [25] and microwave absorbance [26] owing to their electrical conductivity and simple procedure capacity [27]. The combination of PANI with various nanomaterials such as carbon-based materials provides important development for electrochemical applications due to the improved conductivity, stability, and surface area [27,28]. Especially, the interaction of graphene materials with PANI shows extraordinary improvement in sensor/biosensor applications. In addition, GO can be utilized as the conductive substrate and join to MnS crystal and PANI efficiently, providing easy electron transfer.

Sensors/Biosensors have an important feature to decrease the analysis time between sample uptake and the obtained results when these devices can be combined with nanostructured materials. Nanomaterials have been utilized in sensor/biosensor development, microelectronic device production, and catalysis [29,30]. Currently, the core@shell-based nanoparticles have started significant attention [31]. The production methods of these core-shell type magnetic nanoparticles were given in literature such as hydrothermal technique [32], co-precipitation [33] and thermal decomposition [34]. Various core-shell type magnetic nanoparticles were presented such as core Fe_3O_4 and shell gold [35–37]. Especially, AuNPs@Fe_3O_4 has significant advantages such as chemical stability [38], and superior optical, magnetic, and sensor properties [39]. Thus, AuNPs@Fe_3O_4 composite has important applications such as electrochemistry [40], immunosensor preparation [41], and biomolecule separation [38].

Herein, as per the authors' knowledge of the literature, this work is the first that reported an electrochemical tau protein immunosensor based on MnS/GO/PANI and magnetite-incorporated gold nanoparticles. The engineered electrochemical tau protein immunosensor showed some important benefits including superior selectivity, besides outstanding sensitivity, usability, health, and environmental compatibility. Thus, it was highlighted that selective and sensitive electrochemical tau protein immunosensor offered a new approach in terms of Alzheimer's disease diagnosis.

2 Experimental Section

2.1 Materials and Reagents

Antigen Tau, anti-Tau capture antibody (anti-Tau-Ab_1), anti-Tau secondary antibody (anti-Tau-Ab_2), amyloid-beta (Aβ), α-fetoprotein (AFP), bovine serum albumin (BSA), manganese nitrate ($Mn(NO_3)_2$), sodium sulfide (Na_2S), graphite, sodium nitrate ($NaNO_3$), potassium permanganate ($KMnO_4$), sulphuric acid (H_2SO_4), aniline ($C_6H_5NH_2$), ammonium persulphate ($(NH_4)_2S_2O_8$), ferrous chloride ($FeCl_2.4H_2O$), ferric chloride ($FeCl_3.6H_2O$), ethylene glycol (EG), ammonium hydroxide (NH_4OH), sodium citrate ($Na_3C_6H_5O_7$) and hydrogen tetrachloroaurate ($HAuCl_4.3H_2O$) were acquired from Sigma-Aldrich. Moreover, the 0.1 M phosphate-buffered saline (PBS) solution (pH = 7.0) was employed as both supporting electrolyte and dilution buffer solution.

2.2 Instrumentation

ZEISS EVO 50 SEM and JEOL 2100 TEM were used to examine the surface morphologies of materials. The Rigaku X-ray diffractometer with Cu–Kα radiation (λ = 0.154 nm) was employed to acquire x-ray diffraction (XRD) spectra of the nanomaterials. Furthermore, for the evaluation of the electrochemical behavior of the engineered electrodes, Gamry Reference 600 work-station (Gamry, USA) was implemented to conduct cyclic voltammetry (CV), and the electrochemical impedance spectroscopy (EIS), and differential pulse voltammetry (DPV) analysis.

2.3 Fabrication Route of MnS, GO, MnS/GO, and MnS/GO/PANI

The addition of $Mn(NO_3)_2$ (25.0 mM, 20.0 mL) into Na_2S (1.0 M, 25.0 mL) solution was slowly completed at 25 °C during 60 min. The brown precipitate was centrifugated at 10000 rpm to be separated. Afterward, the obtained product ***MnS*** was rinsed with ethanol two times.

GO preparation was carried out according to our previous study in the light of the modified Hummers' method (see Supplementary Data file for detailed information) [42].

$Mn(NO_3)_2$ (10.0 mM, 10.0 mL) solution was prepared in ultra-pure water. Then, Na_2S (2.0 M, 10.0 mL) was added slowly at 25 °C for 60 min. After the addition of the prepared GO (150.0 mg) into the above solution, the brown precipitate (***MnS/GO***) was washed with ultra-pure water and ethanol two times.

The prepared MnS/GO (150.0 mg) was mixed with aniline (2.0 g). Then, $(NH_4)_2S_2O_8$ (75.0 mL) was added slowly into the mixture of MnS/GO:aniline. After homogeneous mixing, the dispersion was washed with the mixture of methanol:ultra-pure water at −5 °C for 4 h. During the preparation of the nanocomposite, the growth of MnS on the GO sheet occurred and during the preparation of the ternary nanocomposite, PANI decorated into the binary precursors (***MnS/GO/PANI)***.

2.4 MnS/GO/PANI Modified GCE (MnS/GO/PANI/GCE) as an Electrochemical Sensor Platform with Anti-Tau-Ab_1 and Antigen Tau Immobilizations

GCE was prepared for the forthcoming use according to the previously reported cleaning procedure (see Supplementary Data file for detailed information) [43]. 20.0 µL of MnS/GO/PANI dispersion (0.2 mg.mL^{-1}) was gently pipetted onto the cleaned GCE surface, followed by drying via infrared heat lamp over 30 min, thereby resulting in MnS/GO/PANI modified GCEs (***MnS/GO/PANI/GCE***). Finally, MnS and MnS/GO modified GCEs (***MnS/GCE*** and ***MnS/GO/GCE)*** were prepared by the same protocol. After preparation of anti-Tau-Ab_1 (25.0 µL, 1.0×10^{-6} M), the anti-Tau-Ab_1 solution was dropped on MnS/GO/PANI/GCE, providing ***anti-Tau-Ab_1/MnS/GO/PANI/GCE*** via stable electrostatic/ionic interactions at 37.0 °C over the period of 20 min. Afterward, BSA (2.0 % w/v) interacted with anti-Tau-Ab_1/MnS/GO/PANI/GCE at the same temperature and the period to remove the non-specific interactions (***BSA/anti-Tau-Ab_1/MnS/GO/PANI/GCE***). After the incubation of antigen Tau proteins having a different concentration on BSA/anti-Tau-Ab_1/MnS/GO/PANI/GCE, the final electrode (***Tau/BSA/anti-Tau-Ab_1/MnS/GO/PANI/GCE***) was washed to remove non-contacting proteins with 0.1 M PBS solution.

2.5 Synthesis of Fe_3O_4NPs, AuNPs, and AuNPs@Fe_3O_4 Composite as Signal Amplification and Anti-Tau-Ab_2 Conjugation

Synthesis of Fe_3O_4NPs was performed by using the co-precipitation technique [44]. The mixture of $FeCl_2\cdot4H_2O$ (25.0 mg) and $FeCl_3\cdot6H_2O$ (35.0 mg) was transferred into the solution of EG:ultra-pure water and stirred at 70 °C. Then, NH_4OH (10 %) was slowly added into the below solution up to pH 10. After washing the dispersion with ultra-pure water two times, the product ***Fe_3O_4NPs*** was stored at 25 °C.

After the preparation of $HAuCl_4.3H_2O$ (20.0 mL, 25.0 mgmL^{-1}) and EG (20.0 mL) mixture, the dispersion was added to Fe_3O_4NPs and stirred for 5 min at 90 °C. Then, sodium citrate (7.0 mL, 0.5 %) was transported to Au^{3+}/Fe_3O_4 solution and stirred for 30 min. The obtained ***AuNPs@Fe_3O_4*** composite was preserved at 25 °C. Finally, **AuNPs** was obtained by the same experimental procedure in our previous study [45].

Following the making ready of anti-Tau-Ab_2 (25.0 µL, 1.0×10^{-6} M), the anti-Tau-Ab_2 solution interacted with AuNPs@Fe_3O_4 composite as a result of strong amino-gold affinity between anti-Tau-Ab_2 and AuNPs@Fe_3O_4 composite[46] and the resultant ***anti-Tau-Ab_2/AuNPs@Fe_3O_4*** was retained in PBS (0.1 M, pH = 7.0).

2.6 Evaluation of the Electrochemical Features of the Electrochemical Immunosensor

The eventual electrochemical Tau immunosensor was formed by the interaction of Tau/BSA/anti-Tau-Ab_1/MnS/GO/PANI/GCE with anti-Tau-Ab_2/AuNPs@Fe_3O_4 via specific antibody-antigen interactions. This interaction was provided by the incubation of 25.0 µL anti-Tau-Ab_2/AuNPs@Fe_3O_4 (20.0 mgmL^{-1}) on Tau/BSA/anti-Tau-Ab_1/MnS/GO/PANI/GCE at immune reaction period of 25 min. Following that, the final Tau immunosensor (***GCE/PANI/GO/MnS/anti-Tau-Ab_1/BSA/Tau/anti-Tau-Ab_2/AuNPs@Fe_3O_4***) was preserved in pH 7.0, 0.1 M PBS (3.0 mL). The reference electrode was an Ag/AgCl/$KCl_{(sat)}$ and the counter electrode was a Pt wire. To monitor electrochemical signals, H_2O_2 as a redox probe was utilized via its conversion into O_2 at about +0.15 V [47,48]. Before the voltammetric experiments, to eliminate the dissolved O2 molecules, the high purity Ar gas was passed through the solution over 20 min. The schematic illustration of the fabrication approach of the electrochemical Tau immunosensor based on the electrochemical reaction mechanism of $H_2O_2 \leftrightarrow O_2 + 2H^+ + 2e^-$ was depicted in Scheme 1.

2.7 Samples Preparation Process

The general procedure for the preparation of the samples was provided in detail in Supplementary Data [49].

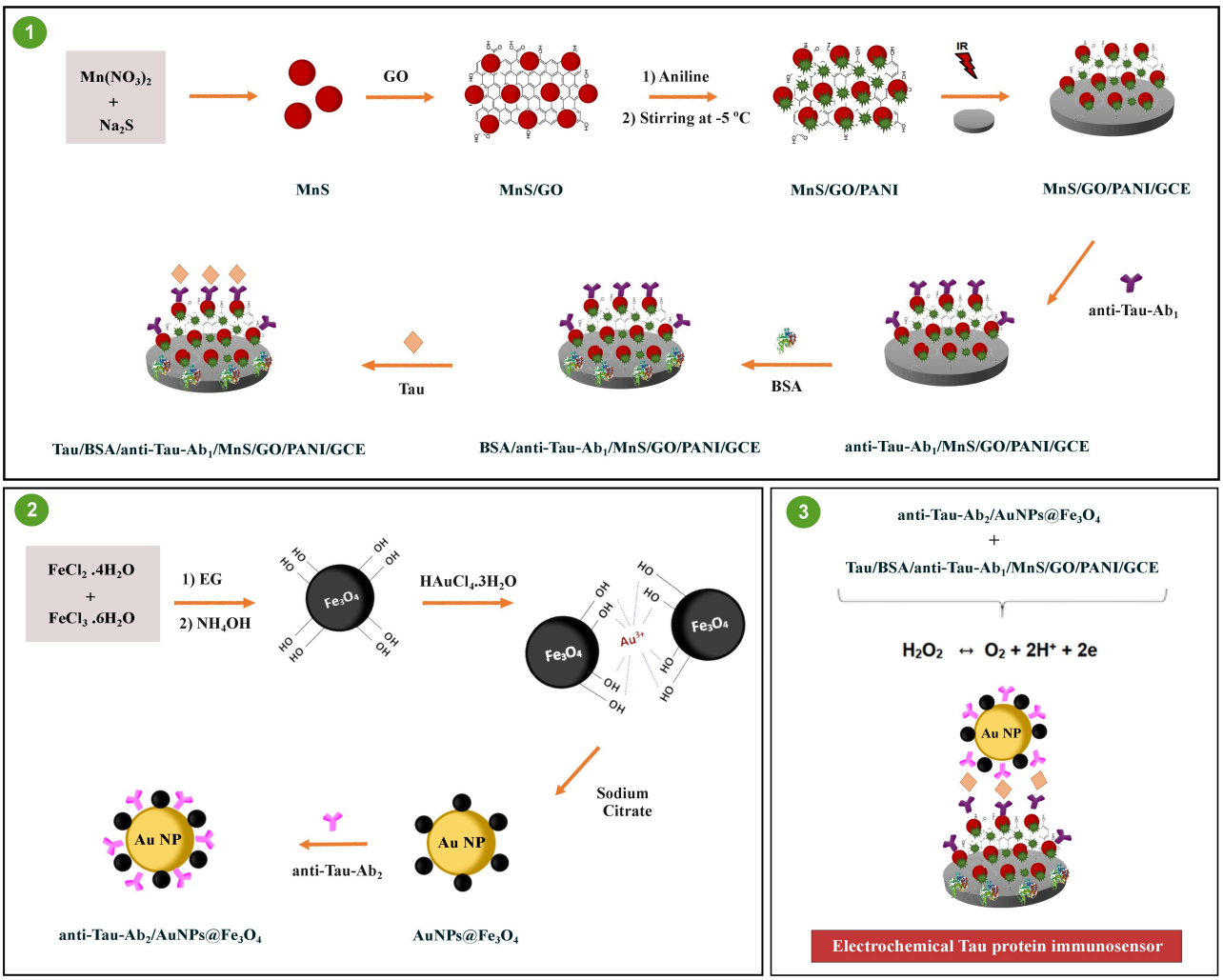

Scheme 1. Schematic representation of the fabrication of electrochemical Tau immunosensor.

3 Results and Discussion

3.1 Morphological and Structural Characterizations of MnS/GO/PANI Electrode Platform

Firstly, the morphological features of MnS, MnS/GO, and MnS/GO/PANI nanocomposite were investigated by scanning electron microscopy (SEM) measurements. According to the growth mechanism, after the ionization of hydrogen sulfide into S^{2-} ions, S^{2-} ions directly reacted with Mn^{2+} ions resulting in the formation of MnS nanoparticles by nucleation process (Figure 1A) [50]. Figure 1B indicated the layered graphene oxide (GO), suggesting homogeneous graphene film including MnS nanoparticles. According to Figure 1B, MnS nanoparticles' regular growth on the GO surface with the amphiphilic macromolecules was observed. This growth was generated on –COOH groups of GO surface. MnS nanoparticles' surface defects and –COOH groups of GO provided the formation of MnS/GO. In addition, –COOH and –C=O– groups of GO served as a support material in MnS nanoparticles structure. SEM image on Figure 1C demonstrated MnS/GO/PANI composite having granular morphology. Due to the interaction between PANI chains and MnS nanoparticles via –NH group, PANI was covalently incorporated into MnS/GO nanocomposites. Then, the cationic PANI was decorated to the anionic GO sheets by electrostatic forces [51]. The incorporation of PANI into MnS/GO nanocomposites provided a ridge-like structure between MnS nanoparticles and GO. This ridge-like structure provides the enhancement of the electron transfer rate on the electrode surface. Hence, the efficient interfacial interaction in nanocomposite structure offered good electrochemical activity in biosensor applications.

Transmission electron microscopy (TEM) characterizations were performed for the detailed morphological investigation of MnS, MnS/GO and MnS/GO/PANI nanocomposite (Figure S1). Figure S1A showed MnS nanoparticles with average particle diameters of 20–25 nm. Figure S1B demonstrated a TEM image of MnS/GO, confirming MnS nanoparticles' formation on GO with 0.24 nm lattice fringes attributing to (200). According to the TEM image of MnS/GO/PANI (Figure S1C), the high

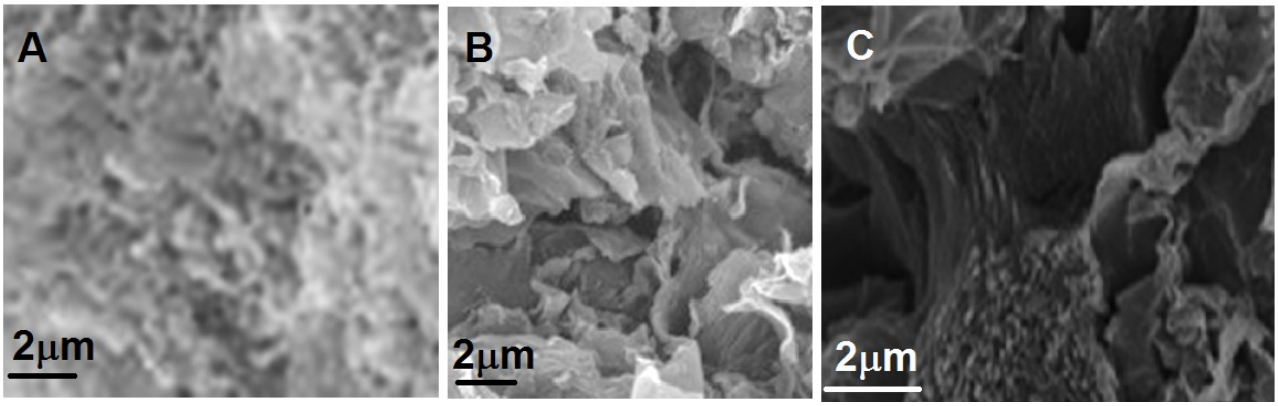

Fig. 1. SEM images of (A) MnS nanoparticles, (B) MnS/GO, (C) MnS/GO/PANI.

stability of GO including MnS nanoparticles and PANI was observed. Hence, efficient electrostatic interaction between MnS nanoparticles and GO and a covalent interaction between GO and PANI provided MnS/GO/PANI nanocomposite having high stability. Especially, the electrostatic and π-π* interactions were nanocomposite formation principles during the ternary preparation containing conducting polymers. In addition, there were many active sites in MnS/GO as a suitable platform for nucleation reaction during PANI formation. Before polymerization, the functional groups such as –COOH and –OH electrostatically interacted with aniline molecules and these aniline molecules started to polymerize on MnS/GO surface [52,53].

Figure S2 demonstrated the obtained Raman spectra for the structural investigations of MnS nanoparticles, MnS/GO and MnS/GO/PANI nanocomposite. Raman bands at 1127, 1333, and 1585 cm^{-1} corresponded to –C–H, –C–N– and –C=C– stretching vibrations, respectively on MnS/GO/PANI spectrum. In the Raman spectrum of MnS/GO, two bands at 1599 and 1364 cm^{-1} were attributed to D and G bands resulting from sp^2 carbon. D band was related to the aromatic ring's breathing mode due to MnS/GO's deformity and the G band was corresponded to sp^2 carbon's bond extending. In addition, PANI incorporation into MnS/GO resulted in the suppression of D and G bands [54]. Finally, the blue shift on D and G bands of MnS/GO/PANI nanocomposite (from 1585 to 1599 cm^{-1}) confirmed strong interaction and electron transfer between PANI and MnS/GO and π-π* interactions between nitrogen electron pairs of PANI and benzene ring of GO formed MnS/GO/PANI nanocomposite.

According to XRD patterns (Figure S3A), the related XRD peaks at 2θ = 25.31, 28.11, and 28.83° corresponded to (100), (002), and (101) planes, respectively, for MnS. 2Θ = 35.81° and 2Θ = 44.03° attributing to (200) and (220) crystal planes indicating α-MnS and ɣ-MnS forms, respectively. Thus, these XRD peaks verified the coexistence of α- and ɣ- phases together in the MnS crystal structure [55]. Two obvious XRD peaks at 2Θ = 19.81° and 2Θ = 24.91° were also attributed to (020) and (200) crystal planes, respectively, for MnS/GO/PANI nanocomposite. In addition, the change in peak intensity and location on the XRD spectrum of MnS/GO/PANI nanocomposite was owing to the migration of the ions in the lattice of MnS [56] and electron charge density intensity from GO to MnS nanoparticle [57].

Fourier transform infrared spectroscopy (FTIR) spectra (Figure S3B) were obtained to verify the presence of MnS nanoparticles, MnS/GO, and MnS/GO/PANI nanocomposite. Firstly, a broad absorption band at about 3400–3500 cm^{-1} was observed on all spectrums, showing the presence of the –OH group. In addition, the absorption bands at 1025 and 1120 cm^{-1} in MnS corresponded to Mn–S bond vibrations and the stretching vibration at about 770 cm^{-1} in MnS was attributed to the Mn–O bond vibrations. The stretching vibrations in GO at 1610, 1090, and 1715 cm^{-1} were related to the –C=C– bond, –C–O–, and –C=O–, respectively. The absorption bands between 2750 and 3000 cm^{-1} confirmed the presence of –C–H bonds. For MnS/GO/PANI nanocomposite, –C=C– bond stretching vibrations were observed at 1570 and 1502 cm^{-1} [58,59]. Aromatic bending vibration at 1150 cm^{-1} was attributed to –C–H. In addition, the absorption bands at 1242 and 1309 cm^{-1} corresponded to polaronic –C–N+ and –C–N groups, respectively [60]. Thus, it was concluded that the successful synthesis of MnS/GO/PANI nanocomposite was completed in the present study.

UV-Vis spectra (Figure S4A) of MnS, MnS/GO, and MnS/GO/PANI were obtained for optical investigations. UV-Vis spectrum of MnS showed that there was an absorption band between 300 and 360 nm. For the UV-Vis spectrum of GO dispersion, the obvious absorption band at 280 nm was corresponded to π-π* transition of –C=C– and the absorption band at 330 nm was attributed to the n-π* transition. Due to interfacial interaction between GO and PANI, there were absorption shifts on UV-Vis spectra of MnS/GO and MnS/GO/PANI. For PANI, a broad peak at 570 nm was attributed to the quinonoid excitation.

Thermogravimetric characterization of MnS/GO/PANI nanocomposite was performed in a nitrogen atmosphere (Figure S4B). Due to the decomposition of hydroxides, a weight loss of about 100 °C occurred. The decomposition of GO's functional groups based on oxygen started at 155 °C and an important weight loss at 390 °C was generated. The oxygen groups' decomposition occurred between 260 and 570 °C. After that, PANI's decomposition started at 210 °C, and GO/PANI showed better thermal stability in comparison with pristine GO or PANI. Hence, PANI grew regularly on GO sheets [61].

Pore sizes and the surface areas of MnS/GO/PANI, MnS/GO and MnS were performed by Brunauer-Emmett-Teller analysis (Figure S5). Figure S5A, B, and C demonstrated N_2 adsorption-desorption isotherms of MnS/GO/PANI, MnS/GO, and MnS with a surface area of 86.3, 40.93, 4.87 $m^2 g^{-1}$, respectively. Owing to PANI incorporation into nanocomposite, the highest surface area was provided for MnS/GO/PANI. The average pore sizes (Figure S5D, E, and F) of MnS/GO/PANI, MnS, and MnS/GO were calculated as 2.94, 3.37, and 4.63 nm, respectively. Due to MnS/GO/PANI having less pore size in comparison with MnS and MnS/GO, polyaniline grew from the pores of the mesopore MnS/GO nanocomposite. Thus, the interfacial interaction in nanostructures provided the easy electrolyte transportation, indicating the improvement of electrochemical performances [62].

3.2 Characterizations of Fe_3O_4NPs, AuNPs, and AuNPs@Fe_3O_4 Composite Signal Amplification

The preparation technique of AuNPs@Fe_3O_4 composite had pristine metal nanoparticles-Fe_3O_4 without any linker, providing the minimal distance between AuNPs and Fe_3O_4 and optimum combination effect. In this technique, EG providing magnetite with hydroxyl groups could facilitate Au^{3+}'s chelation (Au^{3+}/Fe_3O_4) and $Na_3C_6H_5O_7$ as reducing and capping agent could slowly reduce Au^{3+} ions into AuNPs while $Fe^{3+/2+}$ ion pair was not reduced in presence of EG. Thus, the preparation of AuNPs@Fe_3O_4 composite in situ without any linker was successfully completed [63]. According to Figure 2A, the brighter AuNPs was covered by smaller Fe_3O_4NPs. TEM image (Figure 2B) of AuNPs@Fe_3O_4 composite demonstrated that spherical AuNPs with a diameter of 68–75 nm was covered with Fe_3O_4NPs. TEM image (Figure 2C) of Fe_3O_4NPs indicated Fe_3O_4NP a diameter of 10–15 nm. Thus, the successful preparation of AuNPs@Fe_3O_4 composite without any separation was completed as signal amplification in this study. Moreover, the EDX graph

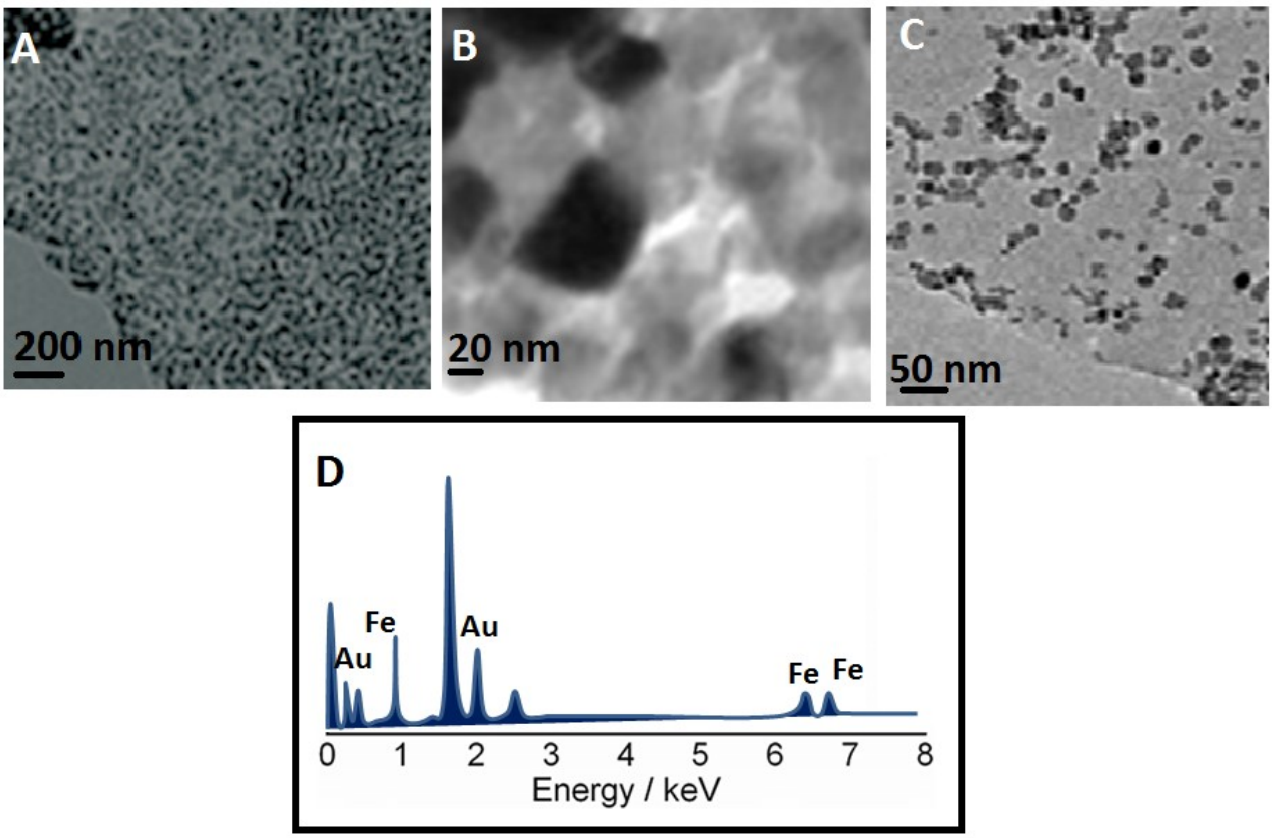

Fig. 2. (A) SEM and (B) TEM image of AuNPs@Fe_3O_4 composite, (C) TEM image of Fe_3O_4NPs, (D) EDX image of AuNPs@Fe_3O_4 composite.

(Figure 2D) confirmed SEM and TEM images by appearing Au and Fe elements.

XRD analysis (Figure S6A) showed XRD patterns of Fe_3O_4NPs and AuNPs@Fe_3O_4 composite. XRD peaks at 30.21°, 35.89°, 43.13°, 57.18°, and 63.08° were corresponded to (220), (311), (400), (511), and (440) planes suggesting Fe_3O_4NPs' cubic inverse structure [64]. At the same time, 38.11°, 44.69°, 65.18°, and 78.11° were attributed to (111), (200), (220), and (311) planes, indicating the cubic AuNPs [65]. Thus, the successful preparation of AuNPs@Fe_3O_4 composite without any change in the magnetite phase was carried out. Figure S6B showed FTIR spectra of Fe_3O_4NPs, AuNPs, and AuNPs@Fe_3O_4 composite. For the FTIR spectrum of Fe_3O_4NPs, a broad absorption band at 3378 cm^{-1} and two absorption bands at 2908 and 2920 cm^{-1} corresponded to –O–H and –C–H groups' vibrations resulting from EG, respectively. Two peaks at 1391 and 571 cm^{-1} corresponded to Fe–O vibrations. For the FTIR spectrum of AuNPs, C=O and –C–H vibrations belonging to sodium citrate at 1728 cm^{-1} and 2905–2920 cm^{-1} were observed. For the FTIR spectrum of AuNPs@Fe_3O_4 nanocomposite, all absorption bands including in FTIR spectra of Fe_3O_4NPs and AuNPs were observed, indicating the successful synthesis of the nanocomposite.

3.3 Evaluation of the Electrochemical Characteristics of the Sensor Platform and Signal Amplification

CV and EIS techniques were conducted to examine the electrochemical characteristics of the as-prepared sensor platform in the presence of 1.0 mM $[Fe(CN)_6]^{3-/4-}$. Primarily, the anodic and the cathodic peaks were observed for bare GCE at around +0.6 V, and +0.4 V, respectively (curve a of Figure 3A). Meanwhile, for the utilization of MnS/GCE (curve b of Figure 3A), the almost same electrochemical activity was observed due to the aggregation of MnS nanoparticles causing poor electrochemical activity [66]. However, when the prepared MnS/GO/GCE (curve c of Figure 3A) and MnS/GO/PANI/GCE (curve d of Figure 3A) were subjected to 1.0 mM $[Fe(CN)_6]^{3-/4-}$, the improved electrochemical activity was observed owing to the high conductive matrix and the no aggregation of nanoparticles [67]. In addition, PANI's electrical conductivity and redox conduct provided increased sensor signals [55]. The predicted decreases in anodic and cathodic signals were produced by the blocking effect of the anti-Tau capture antibody (anti-Tau-Ab_1) (curve e of Figure 3A). Additionally, the immobilizations of BSA (curve f of Figure 3A) and antigen Tau (curve g of Figure 3A) on anti-Tau-Ab_1/MnS/GO/PANI/GCE, respectively, resulted in more electron transfer blocking impact. Hence, the immobilizations of BSA and antigen Tau were effectively achieved, as shown by curves f and g in Figure 3A. Finally, the last immunosensor showed considerable declines in anodic and cathodic signals (curve h of Figure 3A). EIS measurements were gradually carried out to validate CV results (Figure 3B). The charge transfer resistances were computed to be 160 ohm for bare GCE (curve a), 150 ohm for MnS/GCE (curve b), 100 ohm for MnS/GO/GCE (curve c), 80 ohm for MnS/GO/PANI/GCE (curve d), 110 ohm for anti-Tau-Ab_1/MnS/GO/PANI/GCE (curve e), 120 ohm for BSA/anti-Tau-Ab_1/MnS/GO/PANI/GCE (curve f), 130 ohm for Tau/BSA/anti-Tau-Ab_1/MnS/GO/PANI/GCE (curve g) and 140 ohm for the final immunosensor (curve h). As a consequence, we highlighted the fact that CV and EIS findings were in harmony. Finally, two electrochemical Tau immunosensors containing 1.0×10^{-10} M antigen Tau were constructed utilizing distinct signal amplification for the electrochemical assessment of the established signal amplification (Figure 3C). At the 25-minute immune reaction duration, anti-Tau-Ab_2-Fe_3O_4 (curve b of Figure 3C) and anti-Tau-Ab_2-AuNPs@Fe_3O_4

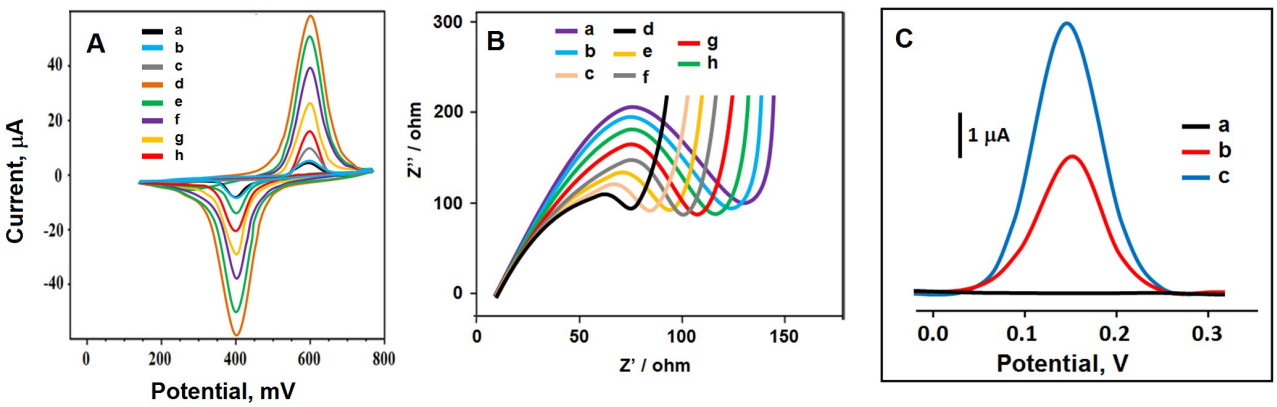

Fig. 3. (A) Cyclic voltammograms, (B) EIS reponses at (a) bare GCE, (b) MnS/GCE, (c) MnS/GO/GCE, (d) MnS/GO/PANI/GCE, (e) anti-Tau-Ab_1/MnS/GO/PANI/GCE, (f) BSA/anti-Tau-Ab_1/MnS/GO/PANI/GCE, (g) Tau/BSA/anti-Tau-Ab_1/MnS/GO/PANI/GCE, (h) the final immunosensor including anti-Tau-Ab_1, antigen Tau and anti-Tau-Ab_2 (scan rate of 100 mV s^{-1}) in 1.0 mM $[Fe(CN)_6]^{3-}$ containing 0.1 M KCl and (C) DPV responses of the developed immunosensors incubated with 1.0×10^{-10} M antigen Tau using anti-Tau-Ab_2-Fe_3O_4 (curve b) and anti-Tau-Ab_2-AuNPs@Fe_3O_4 (curve c) in absence of H_2O_2 (curve a) and in presence of 1.0 mM H_2O_2.

(curve c of Figure 3C) were utilized as signal amplifications. Differential pulse voltammetry signals were recorded in presence of 1.0 mM H_2O_2. As can be seen from Figure 3C, the highest electrochemical immunosensor signals were obtained by anti-Tau-Ab_2-AuNPs@Fe_3O_4 in comparison with anti-Tau-Ab_2-Fe_3O_4 due to the synergistic effect between AuNPs and Fe_3O_4 [68], great catalytic properties and large surface area [69].

3.4 Optimization for Electrochemical Measurements

Detailed optimization studies were investigated in terms of the effect of pH, immune reaction period, hydrogen peroxide, and anti-Tau-Ab_2-AuNPs@Fe_3O_4 solution concentration (Figure S7).

3.5 Linearity Range

The acquired calibration equation (y (μA) = −1.4476x (-logC_{Tau}, M) + 19.902, R^2 = 0.9984) by escalating the concentration of Tau and differential pulse signals were depicted in Figure 4. The quantification limit (LOQ) and LOD were found to be 1.0×10^{-13} M and 1.0×10^{-14} M, respectively. Table 1 illustrated the several characteristics of the constructed electrochemical Tau immunosensor compared to existing Tau analysis methods, such as sensitivity and linearity. It was found that the sensitive electrochemical Tau detection was implemented efficiently in contrast to the other approaches, allowing for the early identification of Alzheimer's disease. In addition, the presented preparation processes of AuNPs@Fe_3O_4 and MnS/GO/PANI composites during immunosensor fabrication was particularly time-saving and magnetite nanoparticles synthesis was specially performed by the co-precipitation method. The linker-free between AuNPs and Fe_3O_4 also provided faster electron transfer and a synergistic effect. The simple and eco-friendly chemicals were also utilized in this preparation method. Lastly, tiny Fe_3O_4 nanoparticles (about 10–15 nm) were obtained, indicating the higher specific surface area and electrochemical activity. Lastly, this developed immunosensor for Tau detection offered an environmentally friendly approach in terms of Alzheimer's disease diagnosis.

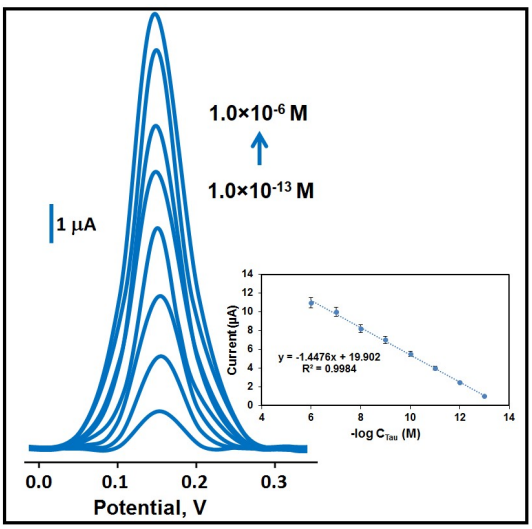

Fig. 4. Concentration effect (from 1.0×10^{-6} to 1.0×10^{-13} M antigen Tau) on immunosensor signals, Inset: Calibration curve for electrochemical Tau immunosensor.

3.6 Selectivity, Stability, and Reproducibility of the Prepared Electrochemical Tau Immunosensor

To demonstrate the superior selectivity of electrochemical immunosensors, four electrochemical Tau immunosensors were developed. Because of this, the developed four electrochemical Tau immunosensors were applied to the prepared protein solutions such as (i) 1.0×10^{-3} M Aβ + 1.0×10^{-3} M AFP + 1.0×10^{-3} M BSA, (ii) 1.0×10^{-6} M Tau + 1.0×10^{-3} M Aβ, (iii) 1.0×10^{-6} M Tau + 1.0×10^{-3} M AFP, (iv) 1.0×10^{-6} M Tau + 1.0×10^{-3} M BSA in presence of 1.0 mM H_2O_2 solution. Figure 5A verified that the other proteins (Aβ, AFP, and BSA) did not affect the high selective electrochemical performance for Tau detection. Furthermore, the great stability of the electrochemical immunosensor was demonstrated by the acquisition of DPV signals (Figure 5B) during a 7-week period. As per Figure 5B, the acquired current signal at the end of the 7th week was about 99.08 % at the end of the first week. These findings suggest the

Table 1. The comparing of some performance metrics for as-fabricated electrochemical Tau immunosensor with other reported approaches.

Material/Method	Linear Range (M)	LOD (M)	Ref.
$CuInS_2$/ZnS	1.0×10^{-11}–2.0×10^{-7}	9.3×10^{-12}	[70]
MWCNTs	1.0×10^{-9}–25.0×10^{-9}	2.0×10^{-9}	[71]
EIS	1.0×10^{-14}–1.0×10^{-8}	3.0×10^{-14}	[72]
Field-effect transistors	1.0×10^{-12}–1.0×10^{-8}	1.0×10^{-12}	[73]
Surface plasmon resonance	1.0×10^{-12}–1.0×10^{-9}	1.0×10^{-12}	[74]
Photoelectrochemical	1.0×10^{-13}–1.0×10^{-10}	1.6×10^{-14}	[75]
Optical aptasensor	2.0×10^{-9}–6.4×10^{-8}	6.7×10^{-9}	[76]
EIS	2.0×10^{-7}–1.0×10^{-6}	2.0×10^{-7}	[77]
Mass Spectrometry	1.0×10^{-9}–5.0×10^{-8}	5.0×10^{-10}	[78]
UHPLC/ESI/MS/MS	1.0×10^{-5}–1.0×10^{-4}	1.0×10^{-5}	[79]
Sandwich type immunosensor	***1.0×10^{-13}–1.0×10^{-6}***	***1.0×10^{-14}***	***This study***

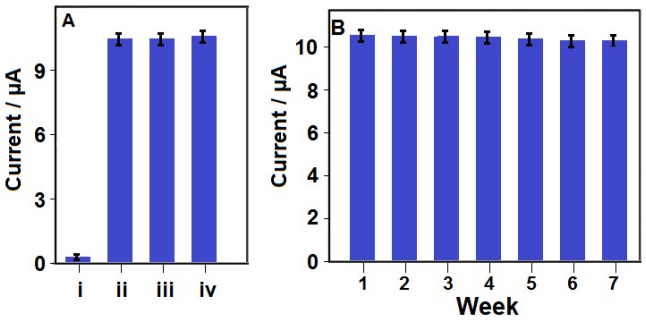

Fig. 5. (A) Immunosensor selective responses against the prepared solutions (n = 6): (i) 1.0×10^{-3} M Aβ + 1.0×10^{-3} M AFP + 1.0×10^{-3} M BSA, (ii) 1.0×10^{-6} M Tau + 1.0×10^{-3} M Aβ, (iii) 1.0×10^{-6} M Tau + 1.0×10^{-3} M AFP, (iv) 1.0×10^{-6} M Tau + 1.0×10^{-3} M BSA; (B) Stability test of electrochemical Tau immunosensor including 1.0×10^{-6} M Tau (n = 6) at 25.0 °C in presence of 1.0 mM H_2O_2.

constructed electrochemical Tau immunosensor's excellent durability. Finally, twenty different electrochemical Tau immunosensors were constructed following the technique in sections 2.4, 2.5, and 2.6 for reproducibility assessment. The relative standard deviation of the measured current signals was determined to be 0.61, demonstrating the high dependability of the immunosensor construction procedure.

4 Conclusions

Analysis of Tau protein as a biomarker of Alzheimer's disease is significant for pathological diagnosis. In the present work, a simple, selective, sensitive, and cheap electrochemical immunosensor was prepared on a glassy carbon electrode via manganese sulfide nanoparticles/graphene oxide/polyaniline sheet to immobilize a specific anti-Tau capture antibody for antigen Tau recognition. The immunosensor showed a highly sensitive detection of antigen Tau with wide linearity (from 1.0×10^{-13} to 1.0×10^{-6} M) and a LOD of 1.0×10^{-14} M, demonstrating the easy utility of the immunosensor in the early detection of Alzheimer's disease at the early stage. The immunosensor indicated a high binding affinity towards antigen Tau in presence of the other interfering proteins.

Acknowledgements

Mehmet Lütfi YOLA thanks Turkish Academy of Sciences for the supports.

Data Availability Statement

The data that supports the findings of this study are available in the supplementary information of this article.

References

[1] C. C. Liu, T. Kanekiyo, H. X. Xu, G. J. Bu, *Nat. Rev. Neurol.* **2013**, *9*(2), 106–118.
[2] C. R. Jack, D. A. Bennett, K. Blennow, M. C. Carrillo, B. Dunn, S. B. Haeberlein, D. M. Holtzman, W. Jagust, F. Jessen, J. Karlawish, E. C. Liu, J. L. Molinuevo, T. Montine, C. Phelps, K. P. Rankin, C. C. Rowe, P. Scheltens, E. Siemers, H. M. Snyder, R. Sperling, C. Elliott, E. Masliah, L. Ryan, N. Silverberg, *Alzheimer's Dementia* **2018**, *14*(4), 535–562.
[3] H. Hampel, S. E. O'Bryant, J. L. Molinuevo, H. Zetterberg, C. L. Masters, S. Lista, S. J. Kiddle, R. Batrla, K. Blennow, *Nat. Rev. Neurol.* **2018**, *14*(11), 639–652.
[4] J. W. Vogel, N. Mattsson, Y. Iturria-Medina, O. T. Strandberg, M. Schöll, C. Dansereau, S. Villeneuve, W. M. van der Flier, P. Scheltens, P. Bellec, A. C. Evans, *Hum. Brain Mapp.* **2019**, *40*(2), 638–651.
[5] L. Qiang, X. Sun, T. O. Austin, H. Muralidharan, D. C. Jean, M. Liu, W. Yu, P. W. Baas, *Curr. Biol.* **2018**, *28*(13), 2181–2189.
[6] C. R. Jack, D. M. Holtzman, *Neuron* **2013**, *80*(6), 1347–1358.
[7] C. Laske, H. R. Sohrabi, S. M. Frost, K. Lopez-de-Ipina, P. Garrard, M. Buscema, J. Dauwels, S. R. Soekadar, S. Mueller, C. Linnemann, S. A. Bridenbaugh, Y. Kanagasingam, R. N. Martins, S. E. O'Bryant, *Alzheimer's Dementia* **2015**, *11*(5), 561–578.
[8] K. Blennow, H. Zetterberg, *Nat. Med.* **2015**, *21*(3), 217–219.
[9] D. L. Sparks, R. J. Kryscio, M. N. Sabbagh, C. Ziolkowski, Y. Lin, L. M. Sparks, C. Liebsack, S. Johnson-Traver, *Am. J. Neurodegener. Dis.* **2012**, *1*(1), 99.
[10] B. Budde, J. Schartner, L. Tonges, C. Kotting, A. Nabers, K. Gerwert, *ACS Sens.* **2019**, *4*(7), 1851–1856.
[11] S. Scarano, S. Lisi, C. Ravelet, E. Peyrin, M. Minunni, *Anal. Chim. Acta* **2016**, *940*, 21–37.
[12] C. Karaman, B. B. Yola, O. Karaman, N. Atar, I. Polat, M. L. Yola, *Microchim. Acta* **2021**, *188*(12), 1–13.
[13] H. Karimi-Maleh, M. L. Yola, N. Atar, Y. Orooji, F. Karimi, P. S. Kumar, J. Rouhi, M. Baghayeri, *J. Colloid Interface Sci.* **2021**, *592*, 174–185.
[14] H. Karimi-Maleh, A. Khataee, F. Karimi, M. Baghayeri, L. Fu, J. Rouhi, C. Karaman, O. Karaman, R. Boukherroub, *Chemosphere* **2022**, *291*, 132928.
[15] H. Karimi-Maleh, F. Karimi, L. Fu, A. L. Sanati, M. Alizadeh, C. Karaman, Y. Orooji, *J. Hazard. Mater.* **2022**, *423*, 127058.
[16] O. Karaman, N. Ozcan, C. Karaman, B. B. Yola, N. Atar, M. L. Yola, *Mater. Today Chem.* **2022**, *23*, 100666.
[17] H. Boyacıoğlu, B. B. Yola, C. Karaman, O. Karaman, N. Atar, M. L. Yola, *Appl. Surf. Sci.* **2022**, *578*, 152093.
[18] C. Karaman, O. Karaman, B. B. Yola, I. Ulker, N. Atar, M. L. Yola, *New J. Chem.* **2021**, *45*(25), 11222–11233.
[19] C. Karaman, O. S. Bolukbasi, B. B. Yola, O. Karaman, N. Atar, M. L. Yola, *Anal. Chim. Acta* **2022**, *1200*, 339609.
[20] L. Zhang, L. Zhou, H. B. Wu, R. Xu, X. W. Lou, *Angew. Chem. Int. Ed.* **2012**, *51*(29), 7267–7270.
[21] C. Ehrenbeck, K. Juttner, *Electrochim. Acta* **1996**, *41*(4), 511–518.
[22] M. Mastragostino, C. Arbizzani, F. Soavi, *J. Power Sources* **2001**, *97–8*, 812–815.
[23] J. Y. Meng, Y. Y. Wang, X. L. Xie, H. Y. Quan, *Ionics* **2019**, *25*(10), 4925–4933.
[24] G. G. Zhang, M. L. Kong, Y. D. Yao, L. Long, M. L. Yan, X. M. Liao, G. F. Yin, Z. B. Huang, A. M. Asiri, X. P. Sun, *Nanotechnology* **2017**, *28*(6), 065402.
[25] K. S. Ryu, K. M. Kim, N. G. Park, Y. J. Park, S. H. Chang, *J. Power Sources* **2002**, *103*(2), 305–309.

[26] E. J. Jelmy, S. Ramakrishnan, N. K. Kothurkar, *Polym. Adv. Technol.* **2016**, *27*(9), 1246–1257.
[27] N. A. Kumar, H. J. Choi, Y. R. Shin, D. W. Chang, L. M. Dai, J. B. Baek, *ACS Nano* **2012**, *6*(2), 1715–1723.
[28] Z. B. Lei, Z. W. Chen, X. S. Zhao, *J. Phys. Chem. C* **2010**, *114*(46), 19867–19874.
[29] C. A. S. Ballesteros, J. Cancino, V. S. Marangoni, V. Zucolotto, *Sens. Actuators B* **2014**, *198*, 377–383.
[30] X. J. Huang, H. S. Im, O. Yarimaga, J. H. Kim, D. H. Lee, H. S. Kim, Y. K. Choi, *J. Phys. Chem. B* **2006**, *110*(43), 21850–21856.
[31] C. J. Zhong, M. M. Maye, *Adv. Mater.* **2001**, *13*(19), 1507–1511.
[32] H. Deng, X. L. Li, Q. Peng, X. Wang, J. P. Chen, Y. D. Li, *Angew. Chem. Int. Ed.* **2005**, *44*(18), 2782–2785.
[33] S. Qiu, L. Xu, Y. R. Cui, Q. P. Deng, W. Wang, H. X. Chen, X. X. Zhang, *Talanta* **2010**, *81*(3), 819–823.
[34] S. H. Sun, H. Zeng, *J. Am. Chem. Soc.* **2002**, *124*(28), 8204–8205.
[35] Z. C. Xu, Y. L. Hou, S. H. Sun, *J. Am. Chem. Soc.* **2007**, *129*(28), 8698–8699.
[36] H. R. Zhang, M. E. Meyerhoff, *Anal. Chem.* **2006**, *78*(2), 609–616.
[37] P. Miao, Y. G. Tang, L. Wang, *ACS Appl. Mater. Interfaces* **2017**, *9*(4), 3940–3947.
[38] H. Y. Park, M. J. Schadt, L. Wang, I. I. S. Lim, P. N. Njoki, S. H. Kim, M. Y. Jang, J. Luo, C. J. Zhong, *Langmuir* **2007**, *23*(17), 9050–9056.
[39] W. Wu, Q. G. He, C. Z. Jiang, *Nanoscale Res. Lett.* **2008**, *3*(11), 397–415.
[40] A. Celebanska, D. Tomaszewska, A. Lesniewski, M. Opallo, *Biosens. Bioelectron.* **2011**, *26*(11), 4417–4422.
[41] Y. Cui, B. Ren, J. L. Yao, R. A. Gu, Z. Q. Tian, *J. Phys. Chem. B* **2006**, *110*(9), 4002–4006.
[42] M. L. Yola, T. Eren, N. Atar, *Electrochim. Acta* **2014**, *125*, 38–47.
[43] M. L. Yola, N. Atar, M. S. Qureshi, Z. Ustundag, A. O. Solak, *Sens. Actuators B* **2012**, *171*, 1207–1215.
[44] M. Sedki, I. A. Khalil, I. M. El-Sherbiny, *Artif. Cells, Nanomed., Biotechnol.* **2018**, *46*, S641–S650.
[45] M. L. Yola, N. Atar, *Electrochim. Acta* **2014**, *119*, 24–31.
[46] B. D. Glisic, U. Rychlewska, M. I. Djuran, *Dalton Trans.* **2012**, *41*(23), 6887–6901.
[47] V. Stankovic, S. Durdid, M. Ognjanovic, J. Mutic, K. Kalcher, D. M. Stankovic, *J. Electroanal. Chem.* **2020**, *876*, 114487.
[48] M. L. Yola, N. Atar, N. Ozcan, *Nanoscale* **2021**, *13*(8), 4660–4669.
[49] M. L. Yola, N. Atar, *Biosens. Bioelectron.* **2019**, *126*, 418–424.
[50] X. Chen, M. He, Y. Zhou, G. He, C. Meng, Q. Cheng, F. Li, *Mater. Today Chem.* **2021**, *21*, 100507.
[51] M. Hassan, K. R. Reddy, E. Haque, S. N. Faisal, S. Ghasemi, A. I. Minett, V. G. Gomes, *Compos. Sci. Technol.* **2014**, *98*, 1–8.
[52] S. Giri, D. Ghosh, C. K. Das, *Adv. Funct. Mater.* **2014**, *24*(9), 1312–1324.
[53] K. V. Sankar, R. K. Selvan, *Electrochim. Acta* **2016**, *213*, 469–481.
[54] Z. S. Yan, J. Y. Long, Q. F. Zhou, Y. Gong, J. H. Lin, *Dalton Trans.* **2018**, *47*(15), 5390–5405.
[55] K. Y. Yasoda, S. Kumar, M. S. Kumar, K. Ghosh, S. K. Batabyal, *Mater. Today Chem.* **2021**, *19*, 100394.
[56] A. Namdarian, A. G. Tabrizi, A. Maseleno, A. Mohammadi, S. E. Moosavifard, *Int. J. Hydrogen Energy* **2018**, *43*(37), 17780–17787.
[57] I. I. Misnon, R. Jose, *New J. Chem.* **2017**, *41*(14), 6574–6584.
[58] M. S. Kumar, P. Das, K. Y. Yasoda, N. K. Kothurkar, S. Malik, S. K. Batabyal, *J. Energy Storage* **2020**, *31*, 101700.
[59] K. R. Reddy, B. C. Sin, K. S. Ryu, J. Noh, Y. Lee, *Synth. Met.* **2009**, *159*(19–20), 1934–1939.
[60] M. Hassan, E. Haque, K. R. Reddy, A. I. Minett, J. Chen, V. G. Gomes, *Nanoscale* **2014**, *6*(20), 11988–11994.
[61] K. R. Reddy, K. P. Lee, A. I. Gopalan, M. S. Kim, A. M. Showkat, Y. C. Nho, *J. Polym. Sci. Polym. Chem. Ed.* **2006**, *44*(10), 3355–3364.
[62] S. D. Yang, C. M. Shen, Y. Y. Liang, H. Tong, W. He, X. Z. Shi, X. G. Zhang, H. J. Gao, *Nanoscale* **2011**, *3*(8), 3277–3284.
[63] J. Olesiak-Banska, M. Gordel, R. Kolkowski, K. Matczyszyn, M. Samoc, *J. Phys. Chem. C* **2014**, *118*(1), 746–746.
[64] Y. L. Li, S. Yang, X. G. Lu, W. Y. Duan, T. Moriga, *RSC Adv.* **2019**, *9*(6), 2877–2884.
[65] S. Krishnamurthy, A. Esterle, N. C. Sharma, S. V. Sahi, *Nanoscale Res. Lett.* **2014**, *9*, 1–9.
[66] R. Ramachandran, M. Saranya, A. N. Grace, F. Wang, *RSC Adv.* **2017**, *7*(4), 2249–2257.
[67] X. C. Dong, X. W. Wang, L. Wang, H. Song, X. G. Li, L. H. Wang, M. B. Chan-Park, C. M. Li, P. Chen, *Carbon* **2012**, *50*(13), 4865–4870.
[68] C. F. Jofre, M. Regiart, M. A. Fernandez-Baldo, M. Bertotti, J. Raba, G. A. Messina, *Anal. Chim. Acta* **2020**, *1096*, 120–129.
[69] Y. L. Yuan, S. S. Li, Y. W. Xue, J. T. Liang, L. J. Cui, Q. B. Li, S. F. Zhou, Y. Huang, G. Y. Li, Y. X. Zhao, *Anal. Biochem.* **2017**, *534*, 56–63.
[70] L. Chen, J. W. Lin, J. Q. Yi, Q. H. Weng, Y. Zhou, Z. Z. Han, C. Y. Li, J. H. Chen, Q. Zhang, *Anal. Bioanal. Chem.* **2019**, *411*(20), 5277–5285.
[71] S. Lisi, S. Scarano, S. Fedeli, E. Pascale, S. Cicchi, C. Ravelet, E. Peyrin, M. Minunni, *Biosens. Bioelectron.* **2017**, *93*, 289–292.
[72] S. X. Y. Wang, D. Acha, A. J. Shah, F. Hills, I. Roitt, A. Demosthenous, R. H. Bayford, *Biosens. Bioelectron.* **2017**, *92*, 482–488.
[73] M. A. Garcia-Chame, O. Gutierrez-Sanz, E. Ercan-Herbst, N. Haustein, M. S. Filipiak, D. E. Ehrnhofer, A. Tarasov, *Biosens. Bioelectron.* **2020**, *159*, 112129.
[74] T. Springer, E. Hemmerova, G. Finocchiaro, Z. Kristofikova, M. Vyhnalek, J. Homola, *Sens. Actuators B* **2020**, *316*.
[75] Y. An, Y. Ren, M. Bick, A. Dudek, E. H. W. Waworuntu, J. Tang, J. Chen, B. S. Chang, *Biosens. Bioelectron.* **2020**, *156*, 112078.
[76] I. Ziu, E. T. Laryea, F. Alashkar, C. L. G. Wu, S. Martic, *Anal. Bioanal. Chem.* **2020**, *412*(5), 1193–1201.
[77] J. O. Esteves-Villanueva, H. Trzeciakiewicz, S. Martic, *Analyst* **2014**, *139*(11), 2823–2831.
[78] M. Y. Xu, M. Y. Lu, W. J. Zhang, Q. W. Jin, Y. Chen, *J. Proteome Res.* **2021**, *20*(5), 2299–2307.
[79] A. Cornejo, F. Salgado, J. Caballero, R. Vargas, M. Simirgiotis, C. Areche, *Int. J. Mol. Sci.* **2016**, *17*(8), 1303.

Received: April 20, 2022
Accepted: April 25, 2022
Published online on ■■, ■■

RESEARCH ARTICLE

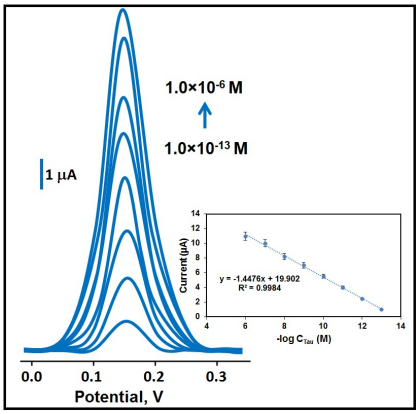

*B. B. Yola, C. Karaman, N. Özcan, N. Atar, İ. Polat, M. L. Yola**